

Numerical Simulations of Solar Energetic Particle Event Timescales Associated with ICMEs

S.-Y. Qi^{1,2}, G. Qin^{3,1,2} and Y. Wang³

¹ State Key Laboratory of Space Weather, National Space Science Center, Chinese Academy of Sciences, Beijing 100190, China

² College of Earth Sciences, University of Chinese Academy of Sciences, Beijing 100049, China

³ School of Science, Harbin Institute of Technology, Shenzhen, 518055, China; qingang@hitsz.edu.cn

Abstract Recently, S.W. Kahler studied the solar energetic particle (SEP) event timescales associated with coronal mass ejections (CMEs) from spacecraft data analysis. They obtained different timescales of SEP events, such as TO , the onset time from CME launch to SEP onset, TR , the rise time from onset to half the peak intensity ($0.5I_p$), and TD , the duration of the SEP intensity above $0.5I_p$. In this work, we solve SEPs transport equation considering ICME shocks as energetic particle sources. With our modeling assumptions, our simulations show similar results to Kahler's spacecraft data analysis that the weighted average of TD increases with both CME speed and width. Besides, from our simulation results, we suggest TD is directly dependent on CME speed, but not dependent on CME width, which were not achieved from the observation data analysis.

Key words: Sun: particle emission — Sun: flare — Sun: coronal mass ejections (CMEs)

1 INTRODUCTION

Solar energetic particle (SEP) events could be mainly divided into two classes through duration and intensity. The short-duration and low-intensity events, which are called impulsive events, are considered to be produced by solar flares. On the other hand, the longer duration and higher intensity ones, which are called gradual events, are considered produced by coronal and interplanetary shocks driven by coronal mass ejections (CMEs). It is interesting to study the relationship between gradual SEP event properties and the characteristics of the associated CMEs. With the first-order Fermi acceleration mechanism (Zank et al., 2000) introduced an onion shell model using a one-dimensional hydrodynamic code for the evolution of the CME-driven shock in the Parker interplanetary magnetic field (IMF). The model is valid only in strong shocks due to Bohm diffusion coefficient used, so Rice et al. (2003) modified it to be usable in arbitrary strengths. In addition, Li et al. (2003) studied the transport of SEPs with their onion shell acceleration model considering particles pitch angle scattering without perpendicular diffusion. In their model, charged particles' pitch angle diffusion is not considered between two consecutive pitch angle scatterings. Furthermore,

Verkhoglyadova et al. (2009, 2010) adopted this model to study individual SEP events caused by CME shocks, their simulation results can fit well with spacecraft observations for different elements. On the other hand, considering that the interplanetary coronal mass ejection (ICME) shocks can continuously accelerate SEPs when propagating outward, Kallenrode & Wibberenz (1997); Kallenrode (2001) treated the ICME shock as a moving particle source. And the model was adopted in a numerical code ¹ by Wang et al. (2012) to study ICME driven shock accelerated particles' transport in three dimensional solar wind and IMF including both parallel and perpendicular diffusion coefficients. Furthermore, under varying perpendicular diffusion and shock acceleration strength, Qin et al. (2013) reproduced the reservoir phenomenon with SPTC numerical simulations. In addition, with the same numerical modeling, Wang & Qin (2015) researched the gradual SEP events spectra focusing on the spatial and temporal invariance. Finally, Qin & Wang (2015) compared the simulation results from SPTC with the multi-spacecraft (*Helios* 1, *Helios* 2, and *IMP* 8) observations during a gradual SEP event, and they obtained the SPTC simulations which best fit the SEP event observed by spacecraft located in different space.

To investigate the relationship between SEP event properties with the associated CMEs, Ding et al. (2014) studied the interaction of two CMEs erupted nearby during a large SEP event by multiple spacecraft observations with the graduated cylindrical shell model. And they obtained the solar particle release time and path length which indicated the necessary influence of the "twin-CME" (Li et al., 2012; Temmer et al., 2012) on the SEP event.

Because of the huge damage caused by SEPs, the study of peak intensities of SEPs becomes very important. Ding et al. (2015) presented the new observation results of peak intensity with Fe/O ratio, which indicate the role of seed population in extremely large SEPs. Reinard & Andrews (2006) studied the dependence of the occurrence and peak intensities of SEP events with CME properties thoroughly using databases of the LASCO/*SOHO* CMEs and the *GOES* $E > 10$ MeV protons. Besides peak intensities, timescales are another very important property of SEPs which could make contribution to both space weather forecasting and understanding of the SEP injection profiles and propagation characteristics.

In order to study the properties and associations of SEP events, Cane et al. (2010) compared SEPs with flares and CMEs of 280 solar proton events which extended above 25 MeV occurred from 1997 to 2006 by near-Earth spacecraft. They divided the events into 5 groups according to the ratios e/p and Fe/O at event onset. Their results suggested that SEP event occurrence and peak intensities are more likely to be associated with faster and wider CMEs, especially with western CME source regions. Furthermore, Pan et al. (2011) investigated SEP timescales, such as the SEP onset time, the SEP rise time, and the SEP duration. With an ice-cream cone model, Pan et al. (2011) studied LASCO/*SOHO* observation data of 95 CMEs associated with SEP events during 1998 – 2002, and came to conclusions that the SEP onset time has no significant correlation with the CME speed, nor with the CME width. They also suggested that the SEP rise time and the SEP duration have significantly positive correlations with the radial speed and angular width of the associated CMEs unless the events are not magnetically well connected to the Earth.

Kahler (2013) did a research on the relationship between the EPACT/*Wind* 20 MeV SEP events timescales and their associated CME speed and widths observed by LASCO/*SOHO*. In Kahler (2013),

¹ Hereafter, we denote the code as Shock Particle Transport Code, SPTC.

217 SEP events observed in a solar cycle during the period 1996-2008 were used. They defined the three characteristic times of the SEP events. The time from inferred CME launch at $1 R_{\odot}$ to the time of the 20 MeV SEP onset at *Wind* was denoted as TO . The time from SEP onset to the time the intensity reached half of the peak value ($0.5I_p$) was denoted as TR . And the time during which the intensity was above $0.5I_p$ was denoted as TD . From their results, they found that CME speed and width were of significant correlation and it is not easy to interpret the contribution of CME speed and width to timescales separately. Therefore, they suggested that faster and wider CMEs which drive shocks and accelerate SEPs over longer times would thus produce the longer SEP timescales TR and TD .

In this paper, with the data used in the analysis of Kahler (2013), we study the CME timescales by numerical simulations with the SPTC, and we compare our results with that of Kahler (2013). In section 2, we present the model. In section 3, we present the data analysis. In section 4, we show our results. In section 5, we present the conclusions and discussion.

2 MODEL

We model the transport of SEPs by following previous research (e.g., Qin et al., 2006; Zhang et al., 2009). The three-dimensional focused transport equation is written as (Skilling, 1971; Schlickeiser, 2002; Qin et al., 2006; Zhang et al., 2009)

$$\begin{aligned} \frac{\partial f}{\partial t} = & \nabla \cdot (\kappa_{\perp} \cdot \nabla f) + \frac{\partial}{\partial \mu} \left(D_{\mu\mu} \frac{\partial f}{\partial \mu} \right) - (v\mu \hat{\mathbf{b}} + \mathbf{V}^{sw}) \cdot \nabla f \\ & + p \left[\frac{1-\mu^2}{2} \left(\nabla \cdot \mathbf{V}^{sw} - \hat{\mathbf{b}} \hat{\mathbf{b}} : \nabla \mathbf{V}^{sw} \right) + \mu^2 \hat{\mathbf{b}} \hat{\mathbf{b}} : \nabla \mathbf{V}^{sw} \right] \frac{\partial f}{\partial p} \\ & - \frac{1-\mu^2}{2} \left[-\frac{v}{L} + \mu \left(\nabla \cdot \mathbf{V}^{sw} - 3 \hat{\mathbf{b}} \hat{\mathbf{b}} : \nabla \mathbf{V}^{sw} \right) \right] \frac{\partial f}{\partial \mu}, \end{aligned} \quad (1)$$

where $f(\mathbf{x}, \mu, p, t)$ is the gyrophase-averaged distribution function, \mathbf{x} is the position in a non-rotating heliographic coordinate system, μ is the particle pitch-angle cosine, p is the particle momentum, v is the particle speed, t is the time, κ_{\perp} and $D_{\mu\mu}$ are the particle perpendicular and pitch-angle diffusion coefficients, respectively, $\mathbf{V}^{sw} = V^{sw} \hat{\mathbf{r}}$ is the solar wind velocity which is in the radial direction, and $L = \left(\hat{\mathbf{b}} \cdot \nabla \ln B_0 \right)^{-1}$ is the magnetic focusing length determined by the magnitude of the background magnetic field B_0 and the unit vector along the local magnetic field $\hat{\mathbf{b}}$. In the equation (1), almost all important transport effects are included, i.e., perpendicular diffusion (1st term in RHS), pitch angle diffusion (2nd term in RHS), particle streaming along field line and solar wind flowing in the IMF (third term in RHS), adiabatic cooling in the expanding solar wind (4th term in RHS), and magnetic focusing in the diverging IMF (5th term in RHS). Here, the drift effects are neglected for lower-energy SEP transport in the inner heliosphere. Also the IMF is modeled with the Parker field.

By following Burger et al. (2008), diffusion coefficients are determined. We set the perpendicular diffusion coefficient from the nonlinear guiding center (NLGC) theory (Matthaeus et al., 2003) approximated with the analytical form according to Shalchi et al. (2004, 2010),

$$\kappa_{\perp} = vl_d^{2/3} \lambda_{\parallel}^{1/3} \left(\mathbf{I} - \hat{\mathbf{b}} \hat{\mathbf{b}} \right), \quad (2)$$

where l_d is a parameter to control the value of the perpendicular diffusion coefficient. For simplicity, κ_{\perp} is set to be independent of μ with the assumption that particle pitch-angle diffusion is much faster than

perpendicular diffusion, but generally μ dependent perpendicular diffusion coefficient should be used (e.g., Qin & Shalchi, 2014b).

The parallel particle mean free path (mfp) λ_{\parallel} is written as (Jokipii, 1966; Hasselmann & Wibberenz, 1968; Earl, 1974)

$$\lambda_{\parallel} = \frac{3v}{8} \int_{-1}^{+1} \frac{(1-\mu^2)^2}{D_{\mu\mu}} d\mu, \quad (3)$$

and parallel diffusion coefficient κ_{\parallel} can be written as $\kappa_{\parallel} = v\lambda_{\parallel}/3$.

We follow Beeck & Wibberenz (1986) and Teufel & Schlickeiser (2003) to model the pitch angle diffusion coefficient

$$D_{\mu\mu}(\mu) = GvR_L^{s-2} \left\{ |\mu|^{s-1} + h \right\} (1 - \mu^2), \quad (4)$$

where G is a parameter to control the value of $D_{\mu\mu}(\mu)$, v is the particle speed, $R_L = pc/(|q|B_0)$ is the particle Larmor radius. Here, a larger value of $h = 0.01$ is chosen for non-linear effect of pitch angle diffusion at $\mu = 0$ in the solar wind (Qin & Shalchi, 2009, 2014a).

To model the particle injection, the shock is treated as a moving SEP source with the boundary condition (Kallenrode & Wibberenz, 1997):

$$f_b = a\delta(r - v_s t) \left(\frac{r}{r_c} \right)^{\alpha} \exp \left[-\frac{|\phi(\theta, \varphi)|}{\phi_c(p)} \right] p^{-\gamma} H(\phi_s - |\phi(\theta, \varphi)|) \quad (5)$$

where α and ϕ_c are the shock acceleration strength parameters. We assume ϕ_c as a constant, but α as a function of shock speed, e.g., we set

$$\alpha = \begin{cases} -3.5 & \text{if } v_s < v_1 \\ v_s/v_0 - 5 & \text{if } v_1 \leq v_s \leq v_2 \\ -2 & \text{if } v_s > v_2 \end{cases} \quad (6)$$

where $v_0 = 500 \text{ km s}^{-1}$, $v_1 = 750 \text{ km s}^{-1}$, and $v_2 = 1500 \text{ km s}^{-1}$. $\phi(\theta, \varphi)$ is the angle between source center and any point of particle injection (θ, φ) . γ is the spectral index of source particles. In the simulations, we inject energetic particle shells with small space intervals Δr . $H(x)$ is the Heaviside step function, with ϕ_s being the half angular width of the shock. A more detailed description of the shock model of our simulations can be referred to Wang et al. (2012).

The transport equation (1) is solved by a time-backward Markov stochastic process method (Zhang, 1999) in the simulations. And the detailed description of the method can be referred to Qin et al. (2006). As mentioned in section 1, our numerical code of transport of energetic particles with the CME driven shock as a moving particle source is denoted as Shock Particle Transport Code, i.e., SPTC.

3 DATA ANALYSIS

We investigate 20 MeV proton intensity-time profiles of SEP events during 1996 to 2008 with their associated CMEs. In particular, the SEP data is from EPACT (the Energetic Particles: Acceleration, Composition, and Transport) (von Rosenvinge et al., 1995) experiment on the *Wind* spacecraft, and the information of their related CMEs is observed by *SOHO* (the *Solar and Heliospheric Observatory* mission) LASCO (Large Angle and Spectrometric Coronagraph) (Brueckner et al., 1995). Of the total 217 SEPs during this period (Kahler, 2013), we study 204 SEPs whose CME parameters are available. In addition, for each event, the CME solar source is determined by flare location, and the speed (v_{CME}) and width (W_{CME}) of CME are obtained from Kahler (2013).

3.1 Parameter Selection

For the grouping and selecting data, we follow the method suggested by Kahler (2013) dividing the 204 events into five longitude ranges with about 41 events each, and subdividing each longitude range into several groups sorted on v_{CME} and W_{CME} , respectively. The median values of longitude, v_{CME} , and W_{shock} in each group are used as the characteristic values.

From data analysis of spacecraft observations, it is not easy to identify SEP onset time accurately which is usually covered by the background of intensity. Therefore, in this work, we only focus on the variation of TD with v_{CME} and W_{CME} . To compare with the observation, we obtain the data analysis results of variation of TD with v_{CME} and W_{CME} from Kahler (2013) as shown in Table 1. From Table 1 we can see, we study SEP events with source location longitude in three ranges, W33–W60, W62–W90, and W100–bWL, with median values W48, W77, and W112, respectively. Note that bWL indicates sources behind the west limbs. In each range of longitude, TD is shown as varying with the median values of v_{CME} and W_{CME} by subdividing the range into several groups sorted on v_{CME} and W_{CME} , respectively.

Table 1 The data analysis results of variation of TD with v_{CME} and W_{CME} from Kahler (2013).

Source Location Longitude	W33-W60		W62-W90		W100-bWL	
	v_{CME} (km/s)	TD (h)	v_{CME} (km/s)	TD (h)	v_{CME} (km/s)	TD (h)
TD varying with v_{CME}	450	6.3	650	6.5	620	13.2
	800	12.0	1150	9.8	900	14.0
	1175	8.8	1450	21.3	1325	12.5
	1600	14.5	2100	18.1	1750	17.0
	W_{CME} (°)	TD (h)	W_{CME} (°)	TD (h)	W_{CME} (°)	TD (h)
TD Varying with W_{CME}	77	8.3	133	7.8	100	7.5
	208	11.3	171	15.0	178	13.3
	360	15.8	360	16.4	360	17.2

In order to study SEP timescales associated with CMEs, we use the SPTC described in Section 2 to simulate the transport of SEPs assuming the CME shock as a moving particle source and that the shock nose is in the flare direction relative to the solar center. In SPTC, the speed of shock, v_s , and the width of shock, W_s , are needed. While, in the spacecraft data analysis of Kahler (2013) the speed and width of CME are used instead. To compare the simulation results with the spacecraft data analysis, we need a model for relationship between v_s and v_{CME} , and that for relationship between W_s and W_{CME} . Firstly, we assume the speed of CME is the same as that of shock, $v_s = v_{CME}$. Secondly, since the width of shock (W_s) is larger than that of CME (W_{CME}), we set,

$$W_s = \begin{cases} W_{CME} + \Delta W & \text{if } W_{CME} < 360^\circ - \Delta W \\ 360^\circ & \text{otherwise.} \end{cases} \quad (7)$$

By testing several value of ΔW , we finally set $\Delta W = 90^\circ$. It is noted that such kind of model for W_s is only an approximation, and it could lead to the discrepancy between the observation and simulation results. So we need to use a better W_s model in the future. Generally, the event source is near the solar equator, so the characteristic latitude of source location is set as 10° north. Other important simulation parameters not varying are shown in Table 2.

Table 2 Model Parameters Used in the Calculations.

Parameter	Physical meaning	Value
E	Particles energy	20 MeV
r_O	Observer solar distance	1 AU
Δr	Shock space interval between two fresh injections	0.001 AU
r_c	Radial normalization parameter	0.05 AU
γ	Spectral index of source particles	-3.5
ϕ_c	Shock strength parameter	15°
λ_{\parallel}^a	Particle mean free path	0.16 AU
$\kappa_{\perp}/\kappa_{\parallel}^a$	Ratio between perpendicular and parallel diffusion coefficient	6.1%
r_{b0}	Inner boundary	0.05 AU
r_{b1}	Outer boundary	50 AU

^a For 20 MeV protons in the ecliptic at 1 AU.

In order to investigate the relationship between solar wind speed v_{SW} and CME speed v_{CME} , we obtain v_{SW} observation data from *Wind* spacecraft for the 204 CME events to fit the relationship between v_{CME} and v_{SW} . It is shown that v_{CME} and v_{SW} are positively correlated. As we assumed above that $v_s = v_{CME}$, the relationship between v_{CME} and v_{SW} would turn to that between v_s and v_{SW} . Thus v_{SW} can be represented by v_s as

$$v_{SW} = 1.77 \times 10^{-5} v_s^2 + 425, \quad (8)$$

here, v_{SW} and v_s are in the unit of km s^{-1} . We also divide the events into several groups sorted on v_{CME} , and obtain the median values of v_{CME} as the characteristic ones for each group. So we obtain the counterpart values v_s and v_{SW} through the assumption above. And we use the characteristic ones in the simulations shown in Table 3. The Table 3 also shows the other input parameters in each simulation coming from the characteristic values of v_{CME} , W_{CME} and source location longitude picked up from Kahler (2013) shown in Table 1.

3.2 Simulation Output

For each data point, 3200000 virtual particles are calculated in our simulations. In our simulations, we obtain the time profiles of SEPs with characteristic speed and width of CME, with which we can get the SEP timescale, TD . For example, in Figure 1, we show simulation results of 20 MeV proton flux during an SEP event. In the simulation of Figure 1, we set solar wind speed as 502.2 km s^{-1} , longitude as 48 degrees west, CME speed as 1600 km s^{-1} , CME width as 180° , other parameters are shown in Table 2. In Figure 1, the dotted line indicates the peak intensity (I_p) of the event, and the dash-dotted line indicates the half peak intensity. T_s and T_e indicate the earliest and latest time when the intensity is half peak, respectively. So we can obtain $TD = T_e - T_s$ from the time profile of intensity of simulation results.

From the results of the simulations we can also get the weighted averages as following. For example, in each range of shock speed and longitude, we have three ranges of shock width, so we have three values

Table 3 Shock speed and width, and solar wind speed used in all simulations.

Source location								
N10W48			N10W77			N10W115		
v_s (km/s)	v_{SW} (km/s)	W_s (°)	v_s (km/s)	v_{SW} (km/s)	W_s (°)	v_s (km/s)	v_{SW} (km/s)	W_s (°)
450	433.5	167	650	433.5	223	620	433.5	190
450	433.5	298	650	433.5	261	620	433.5	268
450	433.5	360	650	433.5	360	620	433.5	360
800	455.4	167	1150	455.4	223	900	455.4	190
800	455.4	298	1150	455.4	261	900	455.4	268
800	455.4	360	1150	455.4	360	900	455.4	360
1175	444.1	167	1450	444.1	223	1325	444.1	190
1175	444.1	298	1450	444.1	261	1325	444.1	268
1175	444.1	360	1450	444.1	360	1325	444.1	360
1600	502.2	167	2100	502.2	223	1750	502.2	190
1600	502.2	298	2100	502.2	261	1750	502.2	268
1600	502.2	360	2100	502.2	360	1750	502.2	360

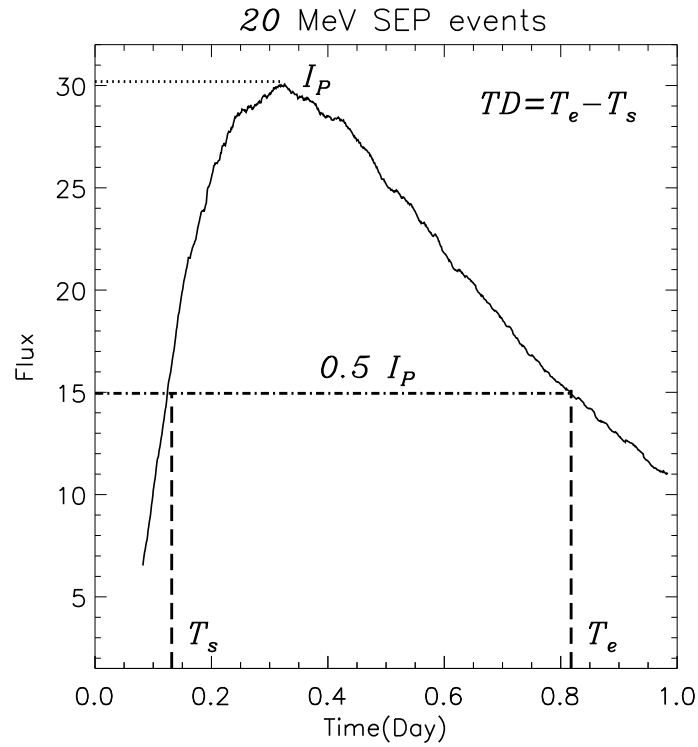


Fig. 1 Flux of 20 MeV proton during an SEP event with parameters shown in the text. The dotted line indicates the peak intensity of the event, and the dash-dotted line indicates the half peak intensity. T_s and T_e indicate the earliest and latest time when the intensity is half peak, respectively.

of TD from simulation results with same shock speed and longitude but different shock width. For the

three ranges of shock width we can get their percentage according to the number of events, with which the weighted value of TD is obtained from the individual values of TD .

Further, we study the relationship between CME speed and CME width using the observation data in Kahler (2013). We subdivide each longitude range into several groups sorted on CME width. We get average CME speed for each group. The results are shown in Figure 2 as the relationship between average of CME speed and the median value of CME width. The three data points in each longitude group of Figure 2 match those of the three CME width bins of Table 1. The line indicates fitting of the data. It is found that in statistics the average CME width increases with the increasing of CME speed.

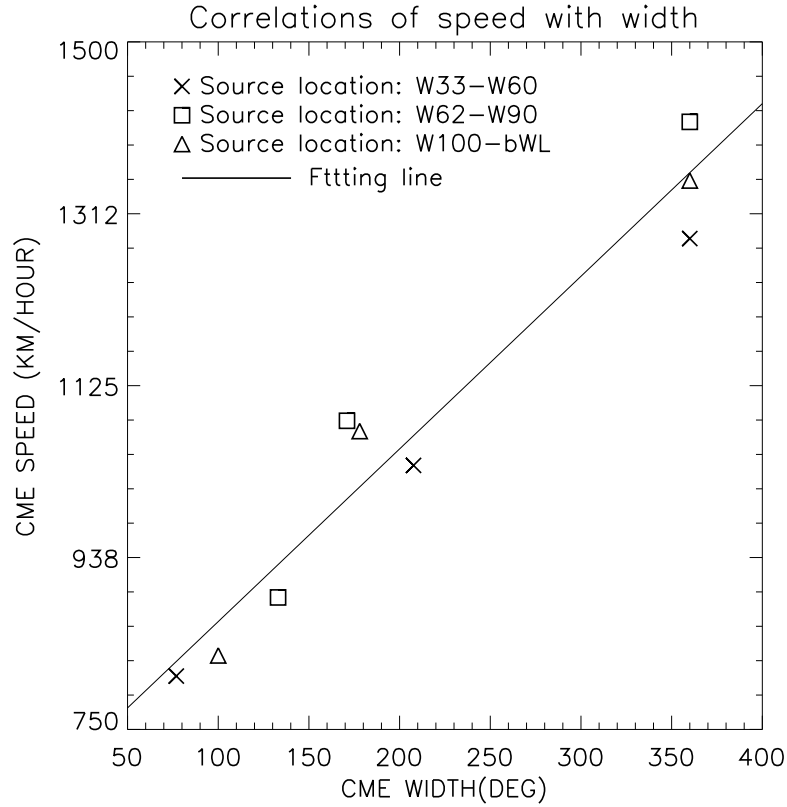


Fig. 2 Variations of CME speed as a function of CME width with different source location. The crosses indicate CME speed averages of the CME width ranges in the source location range of W33–W60, and the squares are that of W62–W90, the triangles are that of W100–bWL. The line indicates fitting of the data. The symbols are from observation data analysed by Kahler (2013).

4 RESULTS

Figure 3 shows SEP timescale TD vs. CME speed for 20 MeV SEP events detected at 1 AU with different source locations in different panels. The top, middle and bottom panels show different longitudes of source locations, 48° west, 77° west, and 115° west, respectively. The black squares indicate spacecraft observation data in Table 1 which are obtained from the data analysis of Kahler (2013). The TD and CME speed for each data points correspond to those of Table 1. The red triangles indicate the weighted average of simulations according to the distribution of number of events with different CME widths for any given CME speed

interval obtained from the observation data in Kahler (2013) corresponding to the the abscissa of black squares. The red and black dashed lines indicate the linear fitting of the weighted average simulation results represented by the red triangles and that of the spacecraft observation data represented by the black squares, respectively. From Figure 3 we can see, the simulation results show the similar trend of observation data, that is, the SEP timescale TD increases with CME speed.

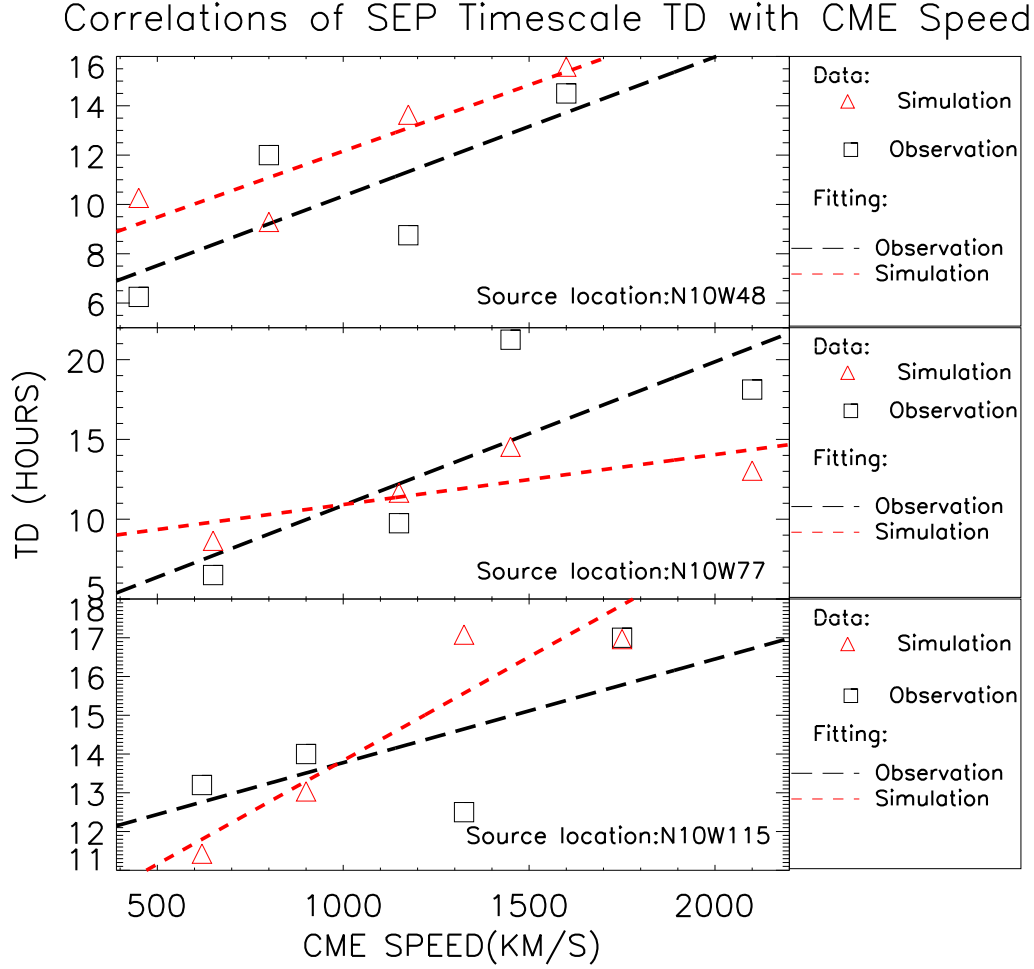


Fig. 3 SEP event timescale TD vs. CME speed. Different panels indicate different source location. The black squares are from observation data analysed by Kahler (2013). The TD and CME speed for each data points correspond to those of Table 1. The red triangles indicate weighted average of simulation results. The black dashed lines indicate linear fitting of observation data. The red dashed lines indicate linear fitting of the weighted average of simulation results.

Figure 4 shows plot similar as Figure 3 except that x-coordinate is CME width. The value for each black squares correspond to those of Table 1. The red triangles indicate weighted average of simulation results according to the distribution of number of events with different CME speeds for any given CME width interval obtained from the observation data in Kahler (2013) corresponding to the abscissa of black squares. Similarly as in Figure 3, the red and black dashed lines indicate the linear fitting of the weighted average

of simulation results and that of the spacecraft observation data, respectively. From Figure 4 we can see, generally, the simulation results show the similar trend of observation data but with less slope, that is, the SEP timescale TD increases with CME width. However, from top panel of Figure 4 (N10W48) it is shown that, the observation results shows the SEP timescale TD increases with CME width, but the simulation results shows constant for different CME width. It is noted that our simulations could show deviation from observations due to modeling and statistical problems.

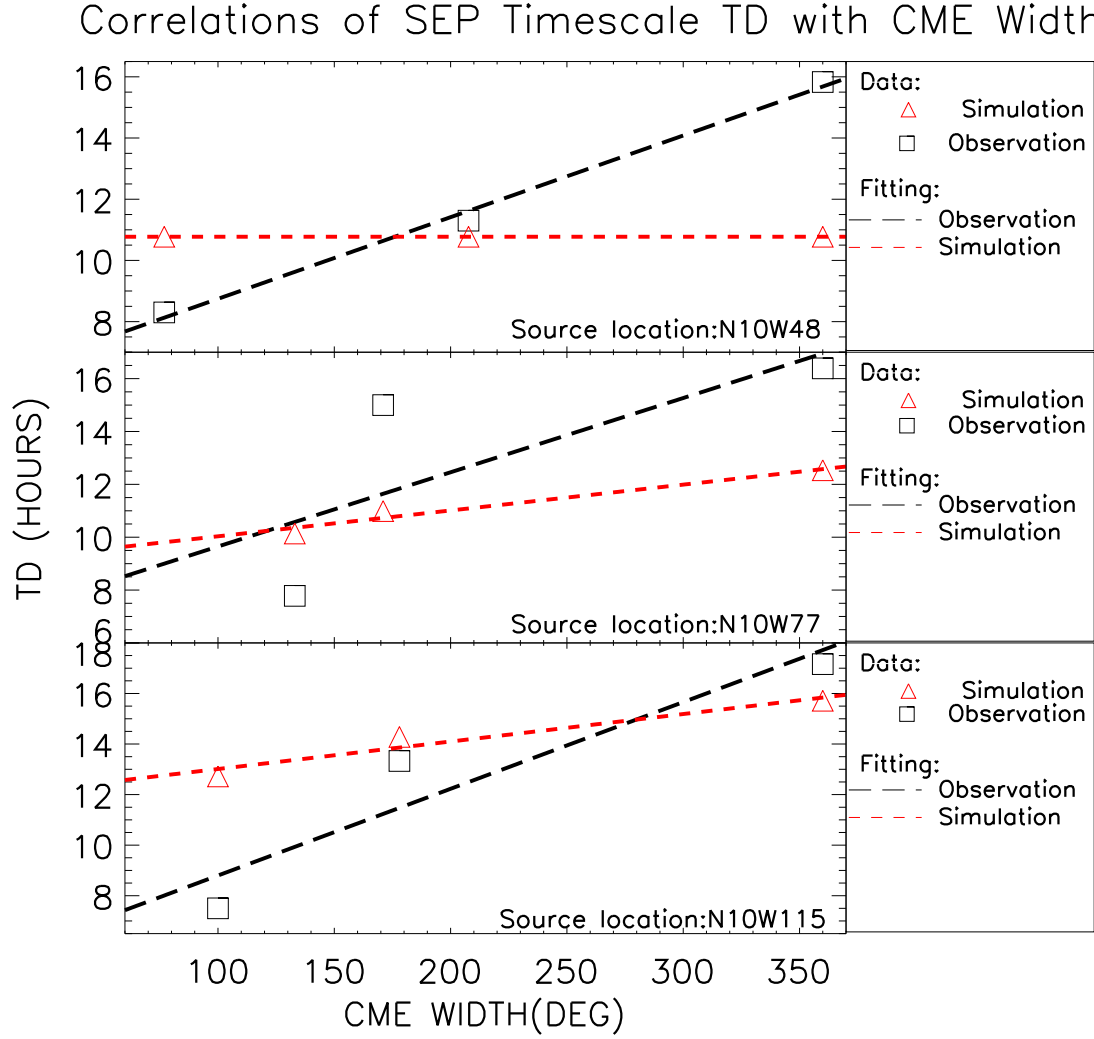


Fig.4 SEP event timescale TD vs. CME width. Different panels indicate different source location. The black squares are from observation data analysed by Kahler (2013). The TD and CME width for each data points correspond to those of Table 1. The red triangles indicate weighted average of simulation results. The black dashed lines indicate linear fitting of observation data. The red dashed lines indicate linear fitting of the weighted average of simulation results.

For further study on the contribution of CME speed and width to timescales separately, we plot the individual simulations and weighted average of simulation results as follows.

Figure 5 shows simulations of SEP timescale TD vs. CME speed for 20 MeV SEP events detected at 1 AU with different source locations in different pannels. Similar as Figure 3, the top, middle and bottom panels show different longitudes of source locations, 48° west, 77° west, and 115° west, respectively. The yellow, green, and blue triangles indicate simulations with different CME widths corresponding to those of Table 1. The each data point of the yellow line shows a individual simulation with a distinct CME speed but a common CME width 133° and source location of N10W48, and so are the green and blue lines with other source location. Besides, the value of all data points are shown in Table 3. The red triangles indicate the weighted average of simulations according to the distribution of number of events with different CME widths for any given CME speed interval obtained from the observation data in Kahler (2013).

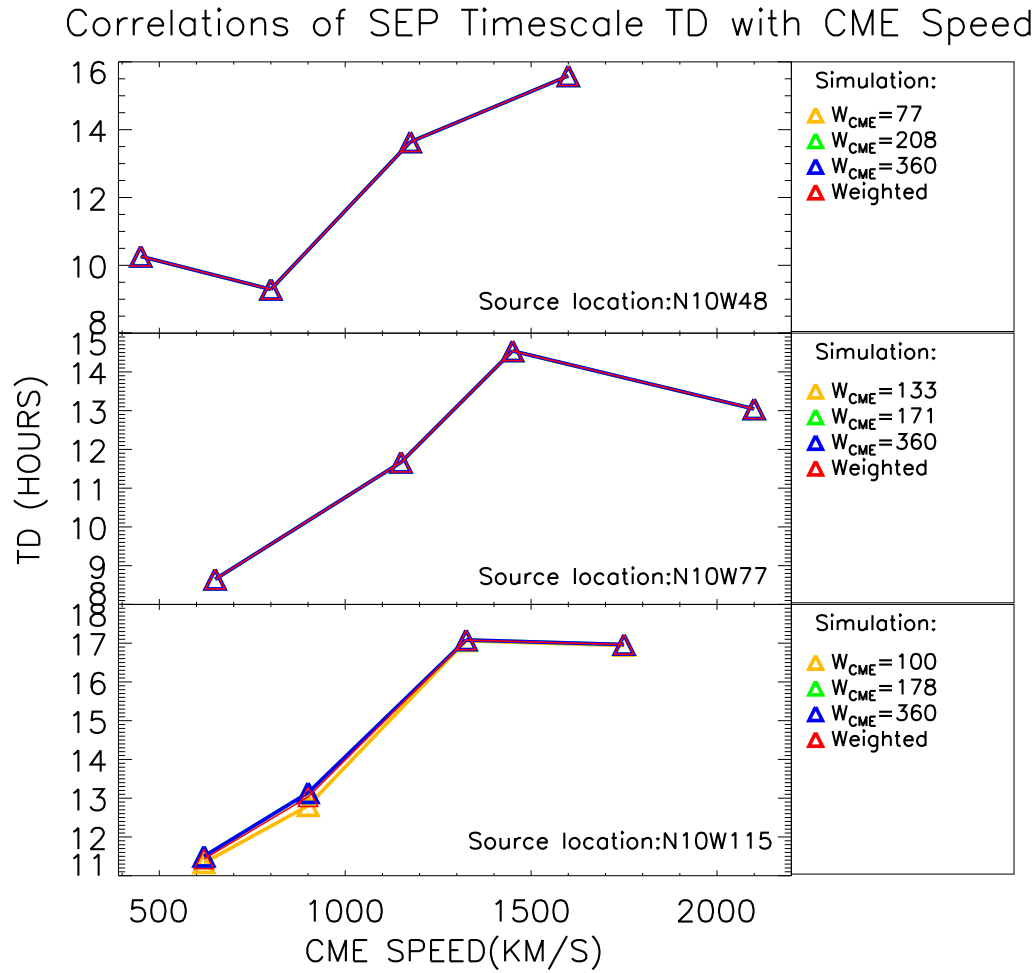


Fig. 5 Simulations of SEP event timescale TD vs. CME speed. Different panels indicate different source location. The yellow, green and blue triangles indicate simulations with different CME widths. The red triangles indicate weighted average of simulation results.

From simulations of Figure 5 we can see, every single colored line increases, that is to say, for the same CME width, TD generally increases with the increasing of CME speed, and the weighted average of TD from simulations also generally increases with the increasing of CME speed. From the other aspect, the

colored lines and symbols are almost overlap, from triangles with a common abscissa but different colors we can see, when CME speed is fixed, TD with different CME widths are almost same, meanwhile, when CME width is fixed, TD with different CME speeds are increased. So we suggest from our simulation that TD is dependent on CME speed but not on CME width, which analysis of Kahler (2013) could not pick out.

Figure 6 shows plot similar as Figure 5 except that x-coordinate is CME width. The yellow, green, light blue and purple triangles indicate simulations with different CME speeds corresponding to those of Table 1. The each data point of the yellow line shows a individual simulation with a distinct CME width but a common CME speed 450 km s^{-1} and source location of N10W48, and so are the green and blue lines with other source location. Besides, the value of all data points are shown in Table 3. The red triangles indicate the weighted average of simulations according to the distribution of number of events with different CME speeds for any given CME width interval obtained from the observation data in Kahler (2013).

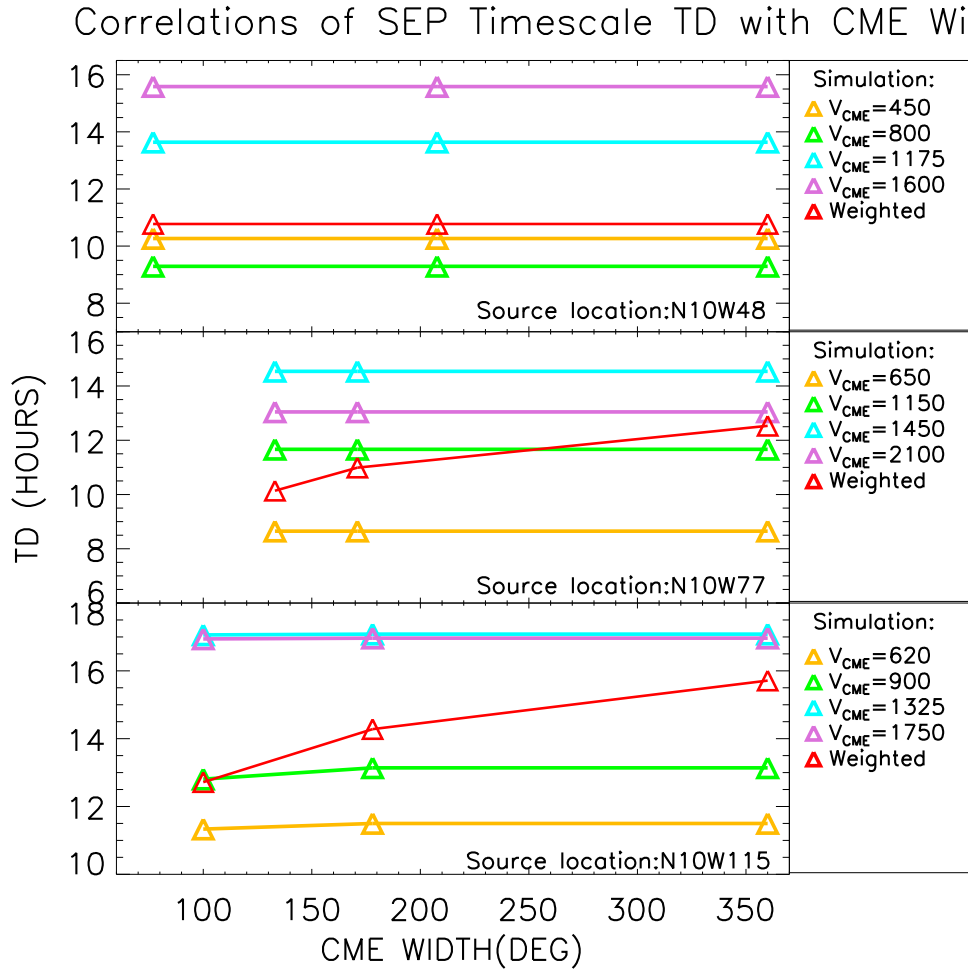


Fig. 6 Simulations of SEP event timescale TD vs. CME width. Different panels indicate different source location. The yellow, green, light blue, and purple triangles indicate simulations with different CME speed. The red triangles indicate weighted average of simulation results.

From simulations of Figure 6 we can see, the yellow, green, light blue and purple lines are almost acclinic, that is to say, for the same CME speed, TD generally keeps constant with different CME width. However, the red line which combines each individual line connecting data points of common CME speed simulations with weighted average increases, that is to say, for the same CME width, TD increases with the increasing of CME speed. In addition, the weighted average of TD increases with the increasing of CME width. The reason is that with larger CME width it is more likely that CME speed becomes larger, so the weighted average of TD becomes larger consequently.

5 CONCLUSIONS AND DISCUSSION

Generally, the accurate measurement of the first arriving particles in SEP events depends on the level of SEP flux background, so usually it is difficult to determine the timescales TR , TO , and $TO + TR$. However, TD , which indicates the duration of the SEP intensity above $0.5I_p$, has nothing to do with the first arriving particles, so the measurements of TD are relatively accurate. Therefore, we only study the timescale TD , but do not study TR , TO , or $TO + TR$.

In this work, we use the SPTC to simulate the transport of SEPs assuming the ICME shock as a moving particle source with parameters obtained from spacecraft observations analysed by Kahler (2013), and other parameters set as typical values of SEP events. From simulations we get SEP timescale TD and compare with TD values from spacecraft data analysis by Kahler (2013). From spacecraft observations shown in Kahler (2013) we obtain the contribution of CME speed with the same CME width, and we also obtain that of CME width with the same CME speed. Finally, from simulation results of TD we can obtain the average of TD weighted with the observations contribution.

Our simulations show that with the same CME speed, TD keeps constant with the increasing of CME width, but that the weighted average of TD increases with the increasing of CME width. From spacecraft data analysis in Kahler (2013) it is shown that TD , which is actually weighted average, increases with the increasing of CME width. In addition, our simulations show that with the same CME width, TD increases with the increasing of CME speed, and that the average of TD increases with the increasing of CME width. It is also shown in Kahler (2013) with spacecraft data analysis that the weighted average of TD increases with the increasing of CME speed. Our simulations generally agree with spacecraft observations data analysis of Kahler (2013) that the weighted average of TD increase with both CME speed and width. Furthermore, with our modeling assumptions, our simulations show some results not shown in Kahler (2013) that TD is dependent directly on CME speed, but independent on CME width.

In order to study whether TD increases with CME width or speed by using observation data, one should choose SEP events with same CME speed but different CME width to show if TD increases with CME width, and also one should choose SEP events with same CME width but different CME speed to show if TD increases with CME speed. Kahler (2013) did not do it because of limitation of events number. But simulations do not have this limitation, and that offers us physical insights behind the observations. We compare the weighted average of simulation to the result of Kahler (2013), and we can show the trend of our weighted average generally agrees with the result of Kahler (2013), so our work do not contradict the

observation result of Kahler (2013). Meanwhile, our individual results can be used to show if TD depends on CME width with same CME speed.

The model we use to calculate flux includes many effects, such as the source, parallel and perpendicular diffusion, adiabatic cooling, etc., the overall effects could be very complicated, so we have to use numerical simulations to get the results. It is possible in some cases TD would decrease. But generally, TD has a trend to increase with the same CME width and increasing CME speed, and TD has a trend to be constant with the same CME speed and increasing CME width. Here, we compare the general trend between observations and simulations.

We choose shock model conditions to favor larger particle injections with increasing speeds and widths in order to compare with observations. There are some parameters arbitrarily chosen and fixed in all simulations, we tried different parameters, for example, we tested simulations with different value of shock strength parameter ϕ_c , such as 10° , 15° , 18° , and 25° , and we found they would not change our general results. In the future, we would continue to study the parameter effects in our model.

The observational evidences of the first detected SEP onsets or releases associated with the good magnetic connection to source were discussed in Ding et al. (2016). Besides, Rouillard et al. (2011, 2012) suggested that SEP onsets could be considered associated with the modeled first connections of field lines to shocks. On the other hand, Qin & Wang (2015) showed the onsets from SPTC simulation results can fit well with that from observations of *HELIOS* 1, *HELIOS* 2, and *IMP* 8 at different longitudes simultaneously with perpendicular diffusion. It is interesting to compare the effects of these models carefully in the future.

There are many authors working on numerical simulations to produce SEP profiles from the shock onion shell model (e.g., Verkhoglyadova et al., 2009, 2010; Wang et al., 2012; Qin et al., 2013), and they usually study the individual SEPs in detail, in this work, however, we are trying to study many SEPs with simulations so we can compare with observations statistically. CME width data from Kahler (2013) were observed by only one satellite, *SOHO*, so they are lack of determinacy. In the future, we would study the CME data of multi-spacecraft observations. In addition, we would study peak intensity of gradual SEP events associated with CMEs by comparing the simulations of SPTC with the spacecraft data analysis (e.g., Kahler & Vourlidas, 2013).

Acknowledgements We are partly supported by grants NNSFC 41304135, NNSFC 41574172, NNSFC 41374177, and NNSFC 41125016, the CMA grant GYHY201106011, and the Specialized Research Fund for State Key Laboratories of China. The computations were performed by Numerical Forecast Modeling R&D and VR System of State Key Laboratory of Space Weather and Special HPC work stand of Chinese Meridian Project. CME data were taken from the CDAW LASCO catalog, which is generated and maintained at the CDAW Data Center by NASA and The Catholic University of America in cooperation with the Naval Research Laboratory. *SOHO* is a project of international cooperation between ESA and NASA. We thank D. Reames for the use of the EPACT proton data.

References

- Beeck, J., & Wibberenz, G. 1986, *Astrophysical Journal*, 311, 437
- Brueckner, G. E., Howard, R. A., Koomen, M. J., et al. 1995, *Solar Physics*, 162, 357

- Burger, R. A., Krüger, T. P. J., Hitge, M., & Engelbrecht, N. E. 2008, *Astrophysical Journal*, 674, 511
- Cane, H. V., Richardson, I. G., & Von Rosenvinge, T. T. 2010, *Journal of Geophysical Research*, 115, A08101
- Ding, L.-G., Cao, X.-X., Wang, Z.-W., & Le, G.-M. 2016, *Research in Astronomy and Astrophysics*, 16, 122
- Ding, L.-G., Li, G., Le, G.-M., Gu, B., & Cao, X.-X. 2015, *The Astrophysical Journal*, 812, 171
- Ding, L.-G., Li, G., Jiang, Y., et al. 2014, *The Astrophysical Journal*, 793, L35
- Earl, J. A. 1974, *The Astrophysical Journal*, 193, 231
- Hasselmann, K., & Wibberenz, G. 1968, *Z. Geophys.*, 34, 353
- Jokipii, J. R. 1966, *The Astrophysical Journal*, 146, 1
- Kahler, S. W. 2013, *The Astrophysical Journal*, 769, 110
- Kahler, S. W., & Vourlidas, A. 2013, *The Astrophysical Journal*, 769, 143
- Kallenrode, M. B. 2001, *Journal of Geophysical Research*, 106, 24989
- Kallenrode, M. B., & Wibberenz, G. 1997, *Journal of Geophysical Research*, 102, 22311
- Li, G., Moore, R., Mewaldt, R. A., Zhao, L., & Labrador, A. W. 2012, *Space Sci. Rev.*, 171, 141
- Li, G., Zank, G. P., & Rice, W. K. M. 2003, *Journal of Geophysical Research*, 108, 1082
- Matthaeus, W. H., Qin, G., Bieber, J. W., & Zank, G. P. 2003, *Astrophysical Journal*, 590, L53
- Pan, Z., Wang, C., Wang, Y., & Xue, X. 2011, *Solar Physics*, 270, 593
- Qin, G., & Shalchi, A. 2009, *Astrophysical Journal*, 707, 61
- Qin, G., & Shalchi, A. 2014a, *Physics of Plasmas*, 21, 231
- Qin, G., & Shalchi, A. 2014b, *Applied Physics Research*, 6, 1
- Qin, G., & Wang, Y. 2015, *The Astrophysical Journal*, 809, 177
- Qin, G., Wang, Y., Zhang, M., & Dalla, S. 2013, *Astrophysical Journal*, 766, 38
- Qin, G., Zhang, M., & Dwyer, J. R. 2006, *Journal of Geophysical Research*, 111, 8101
- Reinard, A. A., & Andrews, M. A. 2006, *Advances in Space Research*, 38, 480
- Rice, W. K. M., Zank, G. P., & Li, G. 2003, *Journal of Geophysical Research Atmospheres*, 108, 1369
- Rouillard, A. P., OdstřCil, D., Sheeley, N. R., et al. 2011, *Astrophysical Journal*, 735, 660
- Rouillard, A. P., Sheeley, N. R., Tylka, A., et al. 2012, *Astrophysical Journal*, 752, 1750
- Schlickeiser, R. 2002, *Cosmic ray astrophysics* (Springer)
- Shalchi, A., Bieber, J. W., Matthaeus, W. H., & Qin, G. 2004, *The Astrophysical Journal*, 616, 617
- Shalchi, A., Li, G., & Zank, G. P. 2010, *apss*, 325, 99
- Skilling, J. 1971, *The Astrophysical Journal*, 170, 265
- Temmer, M., Vrřnak, B., Rollett, T., et al. 2012, *ApJ*, 749, 57
- Teufel, A., & Schlickeiser, R. 2003, *Astronomy & Astrophysics*, 397, 15
- Verkhoglyadova, O. P., Li, G., Zank, G. P., Hu, Q., & Mewaldt, R. A. 2009, *The Astrophysical Journal*, 693, 894
- Verkhoglyadova, O. P., Li, G., Zank, G. P., et al. 2010, *Journal of Geophysical Research*, 115, A12103
- von Rosenvinge, T. T., Barbier, L. M., Karsch, J., et al. 1995, *Space Science Reviews*, 71, 155
- Wang, Y., & Qin, G. 2015, *The Astrophysical Journal*, 806, 252

- Wang, Y., Qin, G., & Zhang, M. 2012, *The Astrophysical Journal*, 752, 37
- Zank, G. P., Rice, W. K. M., & Wu, C. C. 2000, *Journal of Geophysical Research*, 105, 25079
- Zhang, M. 1999, *The Astrophysical Journal*, 513, 409
- Zhang, M., Qin, G., & Rassoul, H. 2009, *The Astrophysical Journal*, 692, 109